Quasiparticle Tunnel Electroresistance in Superconducting Junctions

V. Rouco, Roland El Hage, A. Sander, J. Grandal, K. Seurre, X. Palermo, J. Briatico, S. Collin, J. Trastoy, K. Bouzehouane, et al.

Quasiparticle Tunnel Electroresistance in Superconducting Junctions

V. Rouco[1†], R. El Hage[1], A. Sander[1], J. Grandal[2], K. Seurre[1], X. Palermo[1], J. Briatico[1], S. Collin[1], J. Trastoy[1], K. Bouzehouane[1], A.I. Buzdin[3], G. Singh[4], N. Bergeal[4], C. Feuillet-Palma[4], J. Lesueur[4], C. Leon[2], M. Varela[2], J. Santamaría[1,2] and Javier E. Villegas[1,*]

[1]*Unité Mixte de Physique, CNRS Thales, Université Paris-Sud, Université Paris Saclay, 91767 Palaiseau, France*

[2]*Grupo de Física de Materiales Complejos, Dpt. Física de Materiales, Universidad Complutense de Madrid, 28040 Madrid, Spain*

[3]*Univ Bordeaux, LOMA UMR CNRS 5798, F-33405 Talence, France*

[4]*Laboratoire de Physique et d'Etude des Matériaux, ESPCI Paris, Université PSL, CNRS, 75005 Paris (France)*

The term tunnel electroresistance (TER) denotes a fast, non-volatile, reversible resistance switching triggered by voltage pulses in ferroelectric tunnel junctions. It is explained by subtle mechanisms connected to the voltage-induced reversal of the ferroelectric polarization. Here we demonstrate that effects functionally indistinguishable from the TER can be produced in a simpler junction scheme–a direct contact between a metal and an oxide–through a different mechanism: a reversible redox reaction that modifies the oxide's ground-state. This is shown in junctions based on a cuprate superconductor, whose ground-state is sensitive to the oxygen stoichiometry and can be tracked in operando via changes in the conductance spectra. Furthermore, we find that electrochemistry is the governing mechanism even if a ferroelectric is placed between the metal and the oxide. Finally, we extend the concept of electroresistance to the tunnelling of superconducting quasiparticles, for which the switching effects are much stronger than for normal electrons. Besides providing crucial understanding, those results pave the road towards a new class of Josephson memories.

[†]Current address: Grupo de Física de Materiales Complejos, Dpt. Física de Materiales, Universidad Complutense de Madrid, 28040 Madrid, Spain

* javier.villegas@cnrs-thales.fr

Introduction

Experimental realizations of the tunnel electroresistance[1–5] (TER) have appeared during the last decade in ferroelectric tunnel junctions, which consist of an ultrathin (few nm) ferroelectric tunnel barrier sandwiched between two dissimilar electrodes[3,5] (see Figure 1a for a sketch). In most of the existing experiments, at least one of the involved materials (ferroelectric and/or electrodes) is a complex oxide. These junctions show a characteristic switching between two (or more) non-volatile resistance states that is obtained by applying few-volts pulses across the ferroelectric barrier. Two key functional properties make TER fundamentally different (and technologically interesting) as compared to other resistance-switching phenomena in oxides[6]. First, the conduction mechanism (electron tunnelling) yields sizable current densities at low bias (~mV), which facilitates the non-destructive readout of the resistance states. Second, the resistance switching may be accompanied by a change of the electrode's physical properties[7–10], which enriches the related physics and potential applications. These include novel memories[11] and memristors[12] for neuromorphic computing[13,14].

A series of mechanisms explain the TER under the premise that the applied voltage pulses reverse the ferroelectric polarization[2,15,16]: changes of the orbital hybridization at the junction interfaces (which modify the probability of electron transmission)[2], piezoelectric effects (which modify the tunnel barrier thickness)[17], and effects related to the screening of the polarization charges[15]. The latter effects may operate at two levels. First, because dissimilar electrodes have different Thomas-Fermi screening length λ_{TF}, the height of the energy-barrier across which electrons tunnel depends on whether the ferroelectric polarization points towards one electrode or the other[15]. Second, the electrode's ground state can be modified by the interfacial accumulation of screening electrons[9,18,19]. This so-called ferroelectric field-effect[20] may be relevant for example if (at least) one the electrodes is a strongly correlated material,

such as a manganite[9]. In addition, a debate exists on whether other mechanisms unrelated to ferroelectricity may contribute to the TER, for example the creation of conducting defects within the ferroelectric barrier due to ion electromigration[21,22].

The initial motivation of this work was studying the interplay between superconductivity and TER, using tunnel junctions composed of two superconducting electrodes that sandwich a ferroelectric, and across which superconducting Cooper pairs and quasiparticles may contribute to the conduction. As we will discuss later, the junctions were designed to boost TER mechanisms related to ferroelectric switching that we described above[9,15,18,19]. Unexpectedly, we found that none of these mechanisms are dominant.

In the following, we demonstrate that effects qualitatively and quantitatively identical to the TER are produced instead by a reversible electrochemical (redox) reaction that leads to oxygen exchange between the junction electrodes. This mechanism produces a giant TER in junctions that have a ferroelectric barrier, and also in junctions that consist of two dissimilar electrodes placed in direct contact –i.e. with no third material, ferroelectric or other, placed in between them. Because the redox reaction affects the physical properties of the electrodes, this scenario is different from that of junctions (or capacitors) in which the resistance switching is not in the tunnelling regime and is dominated by electromigration-induced changes within the thick insulating material placed between the electrodes[23–27].The key tool to underpin electrochemistry as the physical mechanism at play is the study of ferroelectric and non-ferroelectric tunnel junctions in which one of the electrodes is a superconducting cuprate. This allows us to correlate the tunnel resistance switching with a modulation of the superconducting energy-gap at the junction interface. The use of a superconducting electrode brings up another key finding; the opening the superconducting energy-gap drastically increases the size of TER effects, which are up to 3000% larger when the current is carried by superconducting quasiparticles than when it is carried by normal electrons.

Results

Junctions' layout and structural characterization

The main experiments were carried out in $Mo_{80}Si_{20}$ (superconductor) / $BiFeO_3$ (ferroelectric) /$YBa_2Cu_3O_{7-\delta}$ (superconductor) micron-size junctions [see scheme in Fig. 1b] fabricated through a combination of pulsed laser deposition, optical lithography and sputtering. $BiFeO_3$ (BFO) doped with Mn (5%) was chosen as ferroelectric barrier. The bottom electrode is $YBa_2Cu_3O_{7-\delta}$ (YBCO), an archetypal high-temperature superconductor with critical temperature T_C~90 K (see supplementary information) on which BFO can be epitaxially grown[28]. This allows for high-quality heterostructures in which the modulation of superconductivity by ferroelectric field-effects[20] has been demonstrated earlier[28] –a priori an interesting ingredient to promote TER. The top electrode, the amorphous alloy $Mo_{80}Si_{20}$ (MoSi), is a low-temperature superconductor (T_C~7 K, see Supplementary Figure 1). As we will see, the superconducting properties of MoSi do not play a role in the present experiments. YBCO and MoSi have very different carrier concentration –respectively ~$3\cdot10^{20}$ cm^{-3} and ~$3\cdot10^{22}$ cm^{-3} –[29,30] and consequently the Thomas-Fermi screening length is expectedly[29] shorter in MoSi (~Å) than in YBCO (~nm). Thus, the pair of electrodes endow the junctions with the asymmetry that expectedly contributes to TER[15] of ferroelectric tunnel junctions. We studied junctions with fixed thickness of MoSi (100 nm) and YBCO (30 nm), and BFO thickness varying from 15 nm to 0 nm (that is, with MoSi and YBCO electrodes in direct contact). Additional control experiments (see Supplementary Figures 3-5) were carried in junctions based on an insulating (non-ferroelectric) $SrTiO_3$ (STO) interlayer instead of BFO, as well as with different counter-electrodes (Au and In_2O_3/SnO_2) instead of MoSi.

A typical scanning transmission electron microscopy (STEM) cross-section image of the junction's interfaces can be seen in Fig. 1c. Atomic resolution high angle annular dark field (HAADF) images show that samples grow epitaxially and the BFO/YBCO interface is

coherent. The top BFO interface shows steps one-unit-cell high, resulting in some physical roughness which does not compromise the BFO layer integrity. The chemical composition can be measured from electron energy-loss spectroscopy (EELS). EELS linescans such as the one in Fig. 1c (top panel) can be obtained by scanning the electron beam across the interface while acquiring EEL spectra. The normalized integrated intensities corresponding to edges of interest such as O, Fe and Ba are shown in the bottom right corner. The O *K* edge signal (in blue) is clearly detected on top of the BFO layer, whose location is depicted by the Fe $L_{2,3}$ edge (red). This O rich layer is extended 2-3 nm into the MoSi layer, which means that a highly oxidized, nanometric MoSi layer right is formed on top of the BFO surface. This finding is not surprising since cuprates have strong tendency to lose oxygen (due to the high reduction potential of Cu^{+3}) and, contrarily, MoSi has a strong tendency to oxidize (stronger than BFO) due to the negative reduction potential of Mo and Si (see Supplementary Table 1). Thus, one expects MoSi to spontaneously oxidize during its growth at the expense of reducing YBCO.

Conductance experiments

Figures 2a through 2c show the differential conductance $G = dI/dV_{BIAS}$ versus applied V_{BIAS} at T = 3.2 K, for junctions with different BFO barrier thickness (see labels). The curves labelled ON were measured after application of a large "poling" voltage V_{pol}>0V, while the curves labeled OFF were measured after V_{pol}<0V. One can see that, for all samples, the conductance is very different in the ON and OFF states. In the ON state, the background dependence is nearly linear, and a "dip" is observed around zero bias. In the OFF state the background is roughly parabolic, and the conductance is down to one order-of-magnitude lower than in the ON state. Indeed, for the sample with thicker BFO (Fig. 2c) the conductance in the OFF state is below the experimental resolution (~10^{-8} S) within the explored bias range.

Figs. 2d-2f display the conductance under bias V_{BIAS}=100 mV and V_{BIAS}=0, namely G_{100} and G_0, measured in the remnant state after application of different V_{pol}. This is cycled

from negative to positive and vice-versa in order to repeatedly switch between the high (ON) and low (OFF) conductance states. The switching is hysteretic, bipolar, and reversible. $G(V_{pol})$ loops are reproducible: each of them contains data from subsequent cycles, which appear superposed. Repeated switching (up to at least one hundred times) produces no significant variation of the ON/OFF conductance levels. Notice that full switching between the two states is obtained for $|V_{pol}|$ in the few-Volts range, and that the loops are asymmetric. That is, a lower $|V_{pol}|$~ 1 V is required to switch from the ON into the OFF state than vice versa, for which V_{pol} ~ 3 V. As shown in Supplementary Figure 4, similar results (size of the resistance switching and switching voltage values) are obtained when the BFO interlayer is substituted by $SrTiO_3$ (a non-ferroelectric band insulator) of similar thickness. However, when MoSi is substituted by a noble-metal (Au) in direct contact with YBCO, the resistance switching is orders-of-magnitude weaker (see Supplementary Figure 3).

Note in Figs. 2d and 2e that the largest resistance switching is observed for low V_{BIAS}. For example, in Fig. 2d, one finds that the electroresistance (defined as $ER \equiv G^{ON}/G^{OFF}$) is ER_0 ~ 5000 at zero bias (see the G_0 loop, dark circles), while it is ER_{100} ~ 150 at V_{BIAS}=100 mV (see the G_{100} loop, light-colored circles). The same bias dependence is evident in Fig. 2e.

Experiments as those described above were conducted for series of junctions with varying dimensions. Fig. 3 shows the relationship between G_{100} (in the ON and OFF states) and the junctions' area A. In the OFF state, the conductance is directly proportional to A (note that the hollow triangles in Figs. 3a and 3b display constant G_{100}/A values), while in the ON state it is not, as already observed in ferroelectric tunnel junctions[31,32]. In fact, in the ON state the conductance is directly proportional to the junctions' perimeter P (note that solid triangles in Figs. 3d, 3e and 3f display constant G_{100}/P values). The scaling observed in the OFF state suggests homogeneous conduction over the junction area, which is consistent with electron tunnelling and rules out current-shunting through conducting defects, such as filaments or

pinholes[6]. The scaling observed in the ON state implies that the resistance switching occurs only over the junction's periphery. As shown earlier[21,31], this can be understood by considering that the electric field produced upon application of V_{pol} is stronger over the edges than in the central area of the junction, favouring the local activation of the switching mechanism. Note that this explanation applies to any electric-field activated switching mechanism[21,31]. For instance, if the mechanism is based on the switching of the ferroelectric polarization, the argument is that the polarization reverses only over the junction' periphery, but remains pinned everywhere else[31]. Finally, from the quantitative point of view, it is worth noticing that the conductance levels $G_{100}/A \sim 10^{-8}$ Sμm^{-2} (OFF state) and $G_{100}/P \sim 10^{-5}$ Sμm^{-1} (ON state) of the 0 nm and 3 nm BFO junctions are comparable to those observed in standard ferroelectric tunnel junctions[31].

In summary, the observed resistance switching characteristics are globally as expected from the extensive literature on TER in ferroelectric tunnel junctions, both qualitatively (shape and symmetry of the switching loops, reversibility, endurance) and quantitatively (switching voltages, size of the conductance switching, scaling with the junctions' size). However, because the behaviour is similar in junctions in which YBCO and MoSi are in direct contact (Figs. 2a, 2d), in junctions with a BFO interlayer, and in junctions with a non-ferroelectric $SrTiO_3$ interlayer (see Supplementary Figure 4), it is evident that ferroelectricity does not play a central role in it. From the phenomenological perspective, there is only one key dissemblance between the observed effects and the TER of oxide-based ferroelectric tunnel junctions: here the electroresistance shows a strong bias dependence which, as revealed by the temperature behaviour discussed below, is connected to superconductivity.

Figs. 2g-2i show G_{100} (light symbols) and G_0 (dark symbols) as a function of temperature, both in the ON (up triangles) and OFF state (down triangles, not measurable for the thickest BFO sample). Notice that the ON and OFF states are set by applying the required

V_{pol} at 3.2 K and the remnant conductance is subsequently measured for increasing temperatures. The temperature dependence of the conductance presents significant differences between different measuring bias. For high bias (G_{100}, light symbols), the behaviour is similar to that of ferroelectric tunnel junctions with normal-metal electrodes[32]: in the ON state, the conductance is nearly constant or slightly decreases with increasing temperature, while in the OFF state it exponentially increases with increasing temperature (see the straight line superposed to the data in Figs. 2g and 2h). The zero-bias conductance (G_0, dark symbols) and G_{100} behave similarly at high temperatures. However, below a given temperature, G_0 drops below the level expected from the high-temperature trend. This departure is weaker in the ON state (see Supplementary Figure 2 for further details) than in the OFF state, for which a pronounced deviation from the exponential dependence (straight line) is observed below ~ 70 K (departure highlighted by the green regions). The above observations imply that, the lower the temperature, the larger the electroresistance $ER \equiv G^{ON}/G^{OFF}$, the enhancement being stronger when measured at zero bias than when measured at 100 mV. Indeed, at low temperatures $ER_0 \gg ER_{100}$. This is clearly observed in the inset of Fig. 2i, which displays ER_0/ER_{100} as a function of temperature for junctions with a 0 nm (black) and 3 nm (red) BFO interlayer. Both curves show a clear upturn below T ~ 70 K, which is more pronounced for the junction with no BFO interlayer (black symbols). For this junction, at the lowest temperature, the zero-bias electroresistance ER_0 is 30 times larger than ER_{100}. As demonstrated below through Fig. 4, this behaviour is explained by the opening of the superconducting energy-gap in YBCO.

Figs. 4a and 4d show the normalized conductance $g(V_{BIAS}) \equiv G(V_{BIAS})/G(60\ mV)$ of the 3 nm BFO sample for different temperatures, respectively in the ON and OFF states. The overall behaviour corresponds to the one typically observed in contacts between a metallic electrode and c-axis YBCO[33,34], and is as expected for quasiparticle tunnelling across a low-

transparency interface (see Supplementary Note 2 for further details). At low temperatures, a "dip" is observed in the low-bias range, in which the conductance drops below the background due to the opening of the superconducting energy-gap[35]. This gap feature is clearer in Figs. 4b and 4e, which respectively display the derivative dg/dV_{BIAS} of the data in 4a and 4d. In both sets of curves (Figs. 4b and 4e) the gap feature clearly stands out from the nearly linear background observed at high temperatures and bias. To better determine the temperature and bias range in which that gap-feature develops, Figs. 4c and 4f show a colour plot of the same data as in 4b and 4e, represented in a different fashion: we plot the ratio between the derivative at the highest T = 140 K, $(dg/dV_{BIAS})^{140K}$, and the derivative at each temperature T, $(dg/dV_{BIAS})^{T}$. Considering the colour scale, green means no deviation from the conductance trend observed at high temperature. The gap-feature stands out in brown colour indicating the conductivity suppression due to the opening of the gap. Direct comparison between Fig. 4c (ON state) and 4f (OFF state) evidences that the superconducting gap opens at lower temperature and within a narrower bias range in the OFF than in the ON state. This data representation allows us to estimate the critical temperature T_C (horizontal dashed line) and gap size Δ (vertical dashed lines). In the ON state, we find T_C~ 90 K and Δ_{YBCO}~ 25 meV, which corresponds to the values expected for optimally doped YBCO. However in the OFF state, T_C ~ 70 K and Δ_{YBCO} ~ 20 meV, which corresponds values for underdoped YBCO. In conclusion, the conductance in the ON state corresponds to tunnelling into optimally doped YBCO, while in the OFF state we observe tunnelling into YBCO with depressed superconducting properties. Thus, the switching between the high (ON) and low (OFF) tunnelling conductance states, driven by the application of V_{pol}, is accompanied by a modulation of the superconductivity in YBCO. Note that the present measurements could not resolve spectral features related with superconductivity in the MoSi electrode, whose energy-gap (Δ_{MoSi} ~ 1 meV) is one order-of-magnitude narrower than YBCO's.

Modelling the electroresistance increase below T_C

The opening of superconducting gap in YBCO leads to a much larger electroresistance $ER \equiv G^{ON}/G^{OFF}$ when measured around zero bias than when measured at 100 mV (compare the loops for G_0 and G_{100} in Figs. 2d and 2e), and to the increase of the ratio ER_0/ER_{100} below $T \sim 70$ K (inset of Fig. 2i). This is because, near zero bias, a significant part of the tunnelling current is carried by quasiparticle excitations. These gradually disappear as the temperature T is decreased below T_C, making the zero-bias conductance G_0 drop. This is illustrated by generalized Blonder-Tinkham-Klapwijk (BTK) theory[8,9] simulations of the junction conductance vs. bias at different temperatures, which are shown in Fig. 5a –see the calculation details in Supplementary Note 3. Notice that both G_0^{ON} and G_0^{OFF} drop with decreasing temperature, as it can be seen in the BTK simulations shown in Fig. 5b, but the drop is more pronounced in the OFF state because[36] the junction's transparency is lower than in the ON state. As a consequence, $ER_0 \equiv G_0^{ON}/G_0^{OFF}$ gradually increases as the temperature is decreased below the T_C in the OFF state. At variance, for eV_{BIAS} = 100 meV >> Δ_{YBCO} the tunnelling current is essentially carried by electrons and therefore G_{100} is unaffected by the quasiparticles population. This results in a weak temperature dependence for ER_{100} , as observed[32] in standard ferroelectric tunnel junctions. All of the above explains the increase of ER_0/ER_{100} observed in the experiments below $T \sim 70$ K (inset in Fig. 2i), which is well captured by the BTK simulations shown in the inset of Fig. 5b.

Origin of the resistance switching

A model of the resistance switching mechanism that accounts for the overall experimental findings is sketched in Fig. 6, which displays a cartoon of the junction's interfaces. The model considers oxygen exchange between YBCO and the junction materials through a reversible redox reaction triggered by V_{pol}. The asymmetry in the switching V_{pol} (Fig. 2d-e and

Supplementary Figure 5) implies that different energy barriers are overcome depending on whether the junction is driven from OFF into ON or vice versa.

Let us start with the case in which there is direct contact between YBCO and MoSi. In the low-conductance state (OFF, Fig. 6a) MoSi is oxidized at the interface (this is labelled $MoSiO_x$) at the expense of leaving behind oxygen vacancies in the YBCO (the oxygen-deficient YBCO is labelled $YBCO_{1-x}$). This is the system's ground-state because, as discussed above, YBCO is the electrode with the highest reduction potential (+2.4V, see Supplementary Table 1). In this state, the interfacial YBCO is severely deoxygenated, which reduces the interface transparency for electrons and quasiparticles, yielding a low junction conductance. The oxygen-deficiency extends beyond the interface, yielding a layer with depressed superconducting properties, as revealed by the smaller energy-gap and low T_C deduced from the tunnelling spectra (Fig. 4f). Upon application of a sufficiently high $V_{pol} > 0$ (Fig. 6b), the redox reaction as reversed. For this process, the highest energy barrier to be overcome –which determines V_{pol} in a first approximation– is given by the difference between the reduction potentials E_0 of MoSi and YBCO. This difference is ΔE_0~ 2.6-3.2 V (see Supplementary Table 1), largely dominated by the high reduction potential of YBCO. This is in good agreement with the switching V_{pol} observed experimentally. The induced redox reaction significantly thins down the oxidized $MoSiO_x$ and oxygen-deficient $YBCO_{1-x}$ layers, with two consequences. First, it yields higher interface transparency and thus higher tunnelling conductance. Second, the YBCO layer becomes optimally doped close to the interface, as shown by $\Delta \sim 25$meV and $T_C \sim 90$K deduced from the tunnelling spectra (Fig. 4c). Application of a $V_{pol} < 0$ returns the junction to back to its ground state (OFF). Notice that in this case the redox reaction is spontaneous from the electrochemical point of view. Thus the only energy barrier to be overcome by V_{pol} is the barrier for ion transport. The fact that all of the junctions show the same ON to OFF switching V_{pol} ~ -1V, regardless of the presence of an interlayer and of the top electrode material (see

Supplementary Figure 5), suggests that the barrier for ion transport arises at the interfacial YBCO layer.

The same electrochemical mechanism can explain the similar effects observed in the presence of a BFO interlayer, only in this case the oxygen exchange that results in the OFF/ON switching involves ion transport across this material. As discussed above and shown by the microscopy (Fig. 1c), an oxidized $MoSiO_x$ layer naturally format the interface, which occurs at the expense of leaving oxygen vacancies in the YBCO because this is by far the material with the highest reduction potential in the stack (see Supplementary Table 1). The switching into the ON state (Fig. 6d) is produced upon application of $V_{pol} > 0$, which moves oxygen back into YBCO. The required $V_{pol} \sim 3$ V is similar as in the absence of BFO interlayer, because it is dominated by the high reduction potential of YBCO. Note however that the reduction potential of BFO is higher than that of MoSi (see Supplementary Table 1). Thus, besides thinning the $MoSiO_x$, the OFF to ON switching process likely involves the creation of oxygen vacancies in BFO, which therefore becomes conducting[24] and contributes to enhancing the junction conductance. Application of $V_{pol} \sim -1$ V drives the junction back to its ground state (OFF) as the barrier for ion transport in YBCO is overcome, allowing for the reaction that oxidizes BFO and MoSi, and leads to YBCO with depressed superconducting properties near the junction interface. In this scenario, as expected, the conductance becomes unmeasurably low in the OFF state for the thicker BFO junctions (Figs. 2c-2f-2i). Notice that, in all cases, oxygen exchange occurs only over the periphery of the junctions, where the electric-field (that assists the redox reaction by activating ion motion) is stronger[21,31]. This explains the perimeter scaling observed in Fig. 3. Further quantitative analysis is shown in Supplementary Figures 6 and 7, including fits of the normal-state tunnel conductance for estimates of the effective tunnel barrier thickness d and height φ. Those yield $d \sim 5$ nm and $\varphi \sim 0.15$ eV for junctions with 0 nm BFO and, consistently, $d \sim 8$ nm and $\varphi \sim 0.53$ eV for junctions with 3 nm BFO. In absence of BFO, the

φ ~ 0.15 eV barrier is due to the decrease in YBCO work function resulting from the electron doping by the oxygen vacancies. The average barrier height φ ~ 0.53 eV in samples with BFO is explained by the difference of the work functions of electron-doped BFO (~4.7eV)[37] and YBCO (~5.2 eV)[38].

Discussion

While redox reactions and the resulting changes in the electrodes' oxidation state may not be the dominant TER mechanism in many of the ferroelectric tunnel junctions studied in the literature, the present study shows that electrochemistry can account for the TER in many cases, in particular if the reduction potential of the involved materials is very different. For instance, materials such as manganites and other transition metal oxides may be prone to reduction when combined with low reduction potential metallic electrodes (e,g, Al or Co). In any case, we show here that functional characteristics of the TER (e.g. the magnitude of the effects, reversibility, endurance, scaling with the device size), and particularly those that make it unique as compared to other resistive switching phenomena (conduction in the tunnelling regime and concomitant manipulation of the electrode's ground-state), can be obtained without the use of ferroelectrics if the junction's electrodes are judiciously chosen. Furthermore, in this case the strongest effects can be achieved if the electrodes are in direct contact, without any barrier material (ferroelectric or other) placed between them. The fact that this demonstration is based on superconductors is interesting, beyond the fact that it allows in operando clear-cut spectroscopic evidence of the oxidation state, because it opens the door to realizing Josephson effects (tunnelling of Cooper pairs) that can be switched between non-volatile states by voltage pulses. These would be of much interest in the field of superconducting electronics[39]**.** While in the present experiments the weak Josephson offered by YBCO –due to its short coherence length along the c-axis– and the high junction resistances have precluded the observation of such effects, extensions of this

work in which the junction interface is along other YBCO crystallographic directions should provide access to them.

Methods

Sample fabrication

Heterostructures with fixed YBCO thickness (30nm) and variable BFO (0 to 15 nm) were grown on $SrTiO_3$ (STO) substrates by pulsed laser deposition, using a KrF 248 nm excimer laser with an energy density of ~1 Jcm^{-2}, and a repetition rate of ~5 Hz. The BFO target was doped with 5%Mn which has been shown to reduce leakage currents in ultrathin films[40]. The homogeneity of the heterostructures was ensured by using a rotating substrate holder. The growth temperatures were 700ºC for YBCO and 560ºC for BFO.A pure oxygen atmosphere (0.36 mbar) was maintained during the subsequent deposition (in situ) of both materials. After BFO growth, the samples were cooled-down in a pure oxygen atmosphere (800 mbar), searching of an optimum oxygen stoichiometry. STEM measurements were carried out in an aberration-corrected JEOL ARM200cF electron microscope operated at 200 kV equipped with a cold field emission gun. Samples were prepared by conventional mechanical grinding and Ar ion milling. Vertical junctions were defined by standard photolithography. A first photoresist layer is spin-coated on top of the heterostructures, in which an array of square holes (that define the junction area A, in the range 10-200 μm^2) is patterned. Following this, the photoresist is hard-baked, so that it becomes immune to subsequent illumination, developing and lift-off processes, and thus permanent. A second photoresist is then spin-coated in order to define an electrical contact pad on top of each of the square holes. An oxygen plasma was used to eliminate all resist residues from the YBCO (or BFO) surface prior to sputtering deposition of a 100 nm thin MoSi film at room temperature, which is followed by the resist lift-off.

Transport measurements

For transport measurements, the voltage applied to the junction is first ramped to V_{pol} (typically up to a few volts) and back to zero. Subsequently, $I(V_{BIAS})$ characteristics are measured at lower voltages ($|V_{BIAS}|$<200 mV). A numerical derivative was performed in order to obtain the

conductance spectra. In all cases, the top electrode (MoSi) was grounded and the voltage was applied to the bottom electrode (YBCO).

Data availability

The data that support the plots within this paper and other findings of this study are available from the corresponding author upon reasonable request.

References

1. Esaki, L., R.B. Laibowitz & P.J. Stiles. Polar switch. *IBM Tech. Discl. Bull.* **13**, 2161 (1971).
2. Tsymbal, E. Y. & Kohlstedt, H. Tunneling across a ferroelectric. *Science* **313**, 181–183 (2006).
3. Garcia, V. *et al.* Giant tunnel electroresistance for non-destructive readout of ferroelectric states. *Nature* **460**, 81–84 (2009).
4. Maksymovych, P. *et al.* Polarization control of electron tunneling into ferroelectric surfaces. *Science* **324**, 1421–5 (2009).
5. Gruverman, A. *et al.* Tunneling electroresistance effect in ferroelectric tunnel junctions at the nanoscale. *Nanoletters* **9**, 3539–3543 (2009).
6. Sawa, A. Resistive switching in transition metal oxides. *Mater. Today* **11**, 28–36 (2008).
7. Garcia, V. *et al.* Ferroelectric control of spin polarization. *Science* **327**, 1106–1110 (2010).
8. Pantel, D., Goetze, S., Hesse, D. & Alexe, M. Reversible electrical switching of spin polarization in multiferroic tunnel junctions. *Nat. Mater.* **11**, 289–293 (2012).
9. Yin, Y. W. *et al.* Enhanced tunnelling electroresistance effect due to a ferroelectrically induced phase transition at a magnetic complex oxide interface. *Nat. Mater.* **12**, 397–402 (2013).
10. Sanchez-Santolino, G. *et al.* Resonant electron tunnelling assisted by charged domain walls in multiferroic tunnel junctions. *Nat. Nanotechnol.* **12**, 655 (2017).
11. Garcia, V. & Bibes, M. Ferroelectric tunnel junctions for information storage and processing. *Nat. Commun.* **5**, 4289 (2014).
12. Chanthbouala, A. *et al.* A ferroelectric memristor. *Nat. Mater.* **11**, 860–864 (2012).
13. Di Ventra, M., Pershin, Y. V. & Chua, L. O. Circuit Elements With Memory: Memristors, Memcapacitors, and Meminductors. *Proc. IEEE* **97**, 1717–1724 (2009).
14. Yang, J. J., Strukov, D. B. & Stewart, D. R. Memristive devices for computing. *Nat. Nanotechnol.* **8**, 13–24 (2013).
15. Zhuravlev, M. Y., Sabirianov, R. F., Jaswal, S. S. & Tsymbal, E. Y. Giant Electroresistance in Ferroelectric Tunnel Junctions. *Phys. Rev. Lett.* **94**, 246802 (2005).
16. Pantel, D. & Alexe, M. Electroresistance effects in ferroelectric tunnel barriers. *Phys. Rev. B* **82**, 134105 (2010).
17. Kohlstedt, H., Pertsev, N. A., Rodriguez Contreras, J. & Waser, R. Theoretical current-voltage characteristics of ferroelectric tunnel junctions. *Phys. Rev. B* **72**, 125341 (2005).
18. Wen, Z., Li, C., Wu, D., Li, A. & Ming, N. Ferroelectric-field-effect-enhanced electroresistance in metal/ferroelectric/semiconductor tunnel junctions. *Nat. Mater.* **12**, 617–621 (2013).
19. Radaelli, G. *et al.* Large room-temperature electroresistance in dual-modulated ferroelectric tunnel barriers. *Adv. Mater.* **27**, 2602–2607 (2015).
20. Ahn, C. H., Triscone, J. & Mannhart, J. Electric field effect in correlated oxide systems. *Nature* **424**, 1015–1018 (2003).
21. Kohlstedt, H. *et al.* Method to distinguish ferroelectric from nonferroelectric origin in case of resistive switching in ferroelectric capacitors. *Appl. Phys. Lett.* **92**, 62907 (2008).
22. Qin, Q. H. *et al.* Resistive Switching in All-Oxide Ferroelectric Tunnel Junctions with Ionic Interfaces. *Adv. Mater.* **28**, 6852 (2016).

23. Szot, K., Speier, W., Bihlmayer, G. & Waser, R. Switching the electrical resistance of individual dislocations in single-crystalline SrTiO3. *Nat. Mater.* **5**, 312–320 (2006).
24. Yang, C. H. *et al.* Electric modulation of conduction in multiferroic Ca-doped BiFeO 3 films. *Nat. Mater.* **8**, 485–493 (2009).
25. Shibuya, B. K., Dittmann, R., Mi, S. & Waser, R. Impact of Defect Distribution on Resistive Switching Characteristics of Sr2TiO4 Thin Films. *Adv. Mater.* **22**, 411–414 (2010).
26. Kwon, D. *et al.* Atomic structure of conducting nanofilaments in TiO2 resistive switching memory. *Nat. Nanotechnol.* **5**, 148–153 (2010).
27. You, T. *et al.* Exploiting Memristive BiFeO 3 Bilayer Structures for Compact Sequential Logics. *Adv. Funct. Mater.* **24**, 3357–3365 (2014).
28. Crassous, A. *et al.* Nanoscale Electrostatic Manipulation of Magnetic Flux Quanta in Ferroelectric/Superconductor BiFeO3/YBa2Cu3O7-δ Heterostructures. *Phys. Rev. Lett.* **107**, 247002 (2011).
29. Mannhart, J. High- Tc transistors. *Supercond. Sci. Technol.* **9**, 49–67 (1996).
30. Banerjee, A. *et al.* Characterisation of amorphous molybdenum silicide (MoSi) superconducting thin films and nanowires. *Supercond. Sci. Technol.* **30**, (2017).
31. Boyn, S. *et al.* Tunnel electroresistance in BiFeO3 junctions: Size does matter. *Appl. Phys. Lett.* **109**, 232902 (2016).
32. Bruno, F. Y. *et al.* Millionfold Resistance Change in Ferroelectric Tunnel Junctions Based on Nickelate Electrodes. *Adv. Electron. Mater.* **2**, 1500245 (2016).
33. Gurvitch, M. *et al.* Reproducible tunneling data on chemically etched single crystals of YBa2Cu3O7. *Phys. Rev. Lett.* **63**, 1008–1011 (1989).
34. Plecenik, A. *et al.* Influence of bias voltage history on conductance properties of YBaCuO/normal metal junctions. *Phys. C Supercond. its Appl.* **301**, 234–242 (1998).
35. Blonder, G. E., Tinkham, M. & Klapwijk, T. M. Transition from metallic to tunneling regimes in superconducting microconstrictions: Excess current, charge invalance, and supercurrent conversion. *Phys. Rev. B* **25**, 4515 (1982).
36. Tinkham, M. *Introduction to Superconductivity*. (Dover Publication Inc., 2004).
37. You, T. *et al.* Engineering interface-type resistive switching in BiFeO3 thin film switches by Ti implantation of bottom electrodes. *Sci. Rep.* **5**, (2015).
38. Dedyk, A. I., Plotkina, N. W. & Ter-Martirosyan, L. T. The Dielectric Hysteresis of YBCO-SrTiO3-YBCO Structures at 4.2 K. *Ferroelectrics* **144**, 77–81 (1993).
39. Rogalla, H. *100 years of superconductivity*. (CRC Press/Taylor & Francis Group, 2012).
40. Zhu, X. H. *et al.* Thickness-dependent structural and electrical properties of multiferroic Mn-doped BiFeO3 thin films grown epitaxially by pulsed laser deposition semiconductor GaAs. *Appl. Phys. Lett.* **93**, 082902 (2008).

Acknowledgements

Work supported by the ERC grant Nº 647100 “SUSPINTRONICS”, French ANR grants ANR-15-CE24-0008-01 “SUPERTRONICS”, and ANR-16-CE24-0028-01 “QUANTUMET”, and European COST action 16218 “Nanocohybri”. Work at UCM supported by Spanish MINECO-FEDER MAT2015-66888-C3-3-R and ERC PoC2016 POLAR-EM and Quantox of QuantERA ERA-NET Cofund in Quantum Technologies (Grant Agreement N. 731473). V. R. acknowledges the European Union’s Horizon 2020 research and innovation programme (Marie Skłodowska-Curie IF grant agreement OXWALD nº 838693). J. S. thanks INP-CNRS and "Scholarship program Alembert" funded by the IDEX Paris-Saclay ANR-11-IDEX-0003-02 for support during his stay at the Unité Mixte de Physique CNRS/Thales. We thank V. Garcia, S. Fusil and A. Barthélémy for discussions and critical reading of the manuscript.

Author Contributions

The study was designed and supervised by JEV. The oxide/metal heterostructures were grown by AS, JB and SC. JG and MV carried out the electron microscopy studies. The junctions were fabricated by VR. The electrical measurements were carried out and analysed by VR with the help of REH. The BTK simulations were performed by KS and XP, with the support of AIB, JL and JEV. The electrochemical model was proposed by VR and developed with contributions from CL and JS. The results were discussed and interpreted by all the authors cited so far, with contributions from JT, KB, GS, NB and CFP. The paper was written by JEV and VR with contributions from all the authors.

Competing Interests

The authors declare no competing interests

Figure 1: Junctions' structure. (a) A tunnel junction whose barrier is ferroelectric can be reversibly switched between a high and low conductance states by the application a voltage pulse of amplitude V_{pol}, which sets the remnant ferroelectric polarization direction towards one electrode or the opposite. **(b)** Scheme of a superconductor/ferroelectric/superconductor tunnel junction based on a $YBa_2Cu_3O_{7-\delta}/BiFeO_3$ heterostructures on which a micrometric $Mo_{80}Si_{20}$ contact is made through an aperture across an insulating photo-resist overlayer. **(c)** (Top) EELS linescan acquired while scanning the electron beam across the stacking, moving a distance *d* from the YBCO into the MoSi layer along the direction of the cyan arrow. The signal intensity is indicated by the color scale (in arbitrary units). The edges of interest include the O *K* edge near 528 eV, Fe $L_{2,3}$ with onset near 709 eV or the Ba $M_{4,5}$, near 781 eV. Principal Component Analysis was used to remove random noise. (Bottom, left) Atomic resolution HAADF image of the YBCO/ BFO/ MoSi stack. Then horizontal dashed lines highlight the approximate locations of the BFO top and bottom interfaces (Bottom, right) Normalized integrated intensities for the O, Fe and Ba signals in blue, red and black, respectively. The vertical dashed lines highlight the approximate locations of the BFO top and bottom interfaces. In all panels a cyan arrow shows the direction of the linescan.

Figure 2: Conductance switching. Differential conductance $G = dI/dV_{BIAS}$ as a function of applied V_{BIAS}, measured at T = 3.2 K after application of $V_{pol} > 0$V (ON state) and $V_{pol} < 0$V (OFF state) for three different BFO thickness **(a)** 0 nm BFO-Mn (V_{pol} = ±3V), **(c)** 3nmBFO-Mn (V_{pol} = +6V and -4V) and **(e)** 15nmBFO-Mn (V_{pol} = ±4V). For the latter thickness, the conductance in the OFF state is unmeasurably low. **(d) (e)** and **(f)** show the switching between the ON and OFF state, This is illustrated by $G_0(V_{pol})$ and $G_{100}(V_{pol})$, that is, the conductance measured at zero bias and at V_{BIAS}=100 mV after application of different V_{pol}, which were cycled repeatedly from negative to positive and vice versa. For the same samples as in (a)-(c).

(g)-(i) show $G_o(T)$ and $G_{100}(T)$ after poling at 3.2 K. The straight lines superposed to the measurements in the OFF state are a extrapolation of the high temperature trend of $G(T)$. Green regions highlight the deviation of $G_o(T)$ from the high temperature trend.

The inset in (i) shows the ratio between the electroresistance ($ER = G_{ON}/G_{OFF}$) at zero bias and that under V_{BIAS}=100 mV, that is ER_0/ER_{100}, as a function of temperature for the 0 nm BFO (diamonds), and 3 nm BFO junction (squares symbols). ER_0/ER_{100} is calculated from the data in 2g and 2h. The green region highlights the deviation of ER_0/ER_{100} from the high temperature trend. The vertical axis presents a break between ER_0/ER_{100} = 10 and ER_0/ER_{100} = 25.

Figure 3: Scaling of the conductance with the junctions' size. For a series of junctions with variable area A: **(a,b,c)** $G_{100}(3.2K)$ in the ON and OFF states normalized by the junction area,G_{100}/A; and **(d,e,f)** $G_{100}(3.2K)$ in the different states normalized by the junction perimeter, G_{100}/P for the different samples. Lines are a guide to the eye.

Figure 4. Temperature dependence of the spectral features. For a the 3nm BFO junction, in the ON state **(a)** and OFF state **(d):** differential conductance normalized to the conductance at 60 mV, $G(V_{BIAS})/G_{60mV}$, for different temperatures in the series 3.2, 4, 5, 6, 7, 8, 9, 10, 20, 40, 60, 80, 90, 100, 120, 140 K, which correspond to the different curve colours. The series extrema are indicated by the labels. **(b)** and **(e)** respectively show the first derivative dG/dV_{BIAS} of those curves. **(c)** and **(f)** shows the ratio between the dg/dV_{BIAS} at T = 140 K and dg/dV_{BIAS} at any other temperature. as a function of the bias voltage and temperature. The range V_{BIAS} < 5 mV is masked because the ratio between two values close to zero yields a too large data scattering. The vertical dashed lines show the bias span of the gap feature, the horizontal dashed lines point the critical temperature at which the gap starts opening.

Figure 5. BTK modeling of the temperature dependent quasiparticle tunnel electro-resistance. (a) Example of the BTK conductance *vs*. bias at different temperatures for a set of parameters (indicated in the legend) that correspond to the ON state. G_0 and G_{100} are respectively indicated by the dark/light triangles. (b) $G_0(T)$ (dark triangles) and $G_{100}(T)$ (light triangles) calculated in the ON and OFF state using the BTK parameter indicated in the legend. Notice that $G_0(T)$ gradually drops below $G_{100}(T)$ as temperature is decreased beyond T_C, which is highlighted by the green regions. The departure is more pronounced than in the OFF state that in the ON state. The inset shows the ratio ER_0/ER_{100} as deduced from the calculations shown in the main panel. Notice the steady increase below the critical temperature in the OFF state (T_C = 70 K), highlighted by the green region.

Figure 6. Electro-resistance model based on electrochemistry. Schematic representation of the junctions with and without BFO. The oxygen anion (O^{-2}; black dots) and oxygen vacancy (${V_O}^{+2}$; hollow dots) distributions are indicated. **(a)** OFF state of the 0nm BFO junctions. The bottom electrode shows a gradual oxygen depletion (and thus depressed superconducting properties) which is very strong near the interface due to the interfacial oxidation ($MoSiO_x$) of the top MoSi electrode. **(b)** By applying $V_{pol} > 0$, O^{-2} migrate downwards and the oxygen depletion is much more confined near the interface, leaving optimally doped YBCO. This occurs on the junction's' edges, where the electric field is stronger. **(c)** OFF state of the junctions with BFO, in which YBCO shows gradual oxygen depletion (and thus depressed superconducting properties) which is very strong near the interface. In this state BFO is not significantly oxygen deficient. **(d)** By applying $V_{pol} > 0$ (ON state), oxygen vacancies${V_O}^{+2}$

migrate into de BFO, resulting in a fully oxygenated YBCO and in oxygen-depleted, conducting BFO.

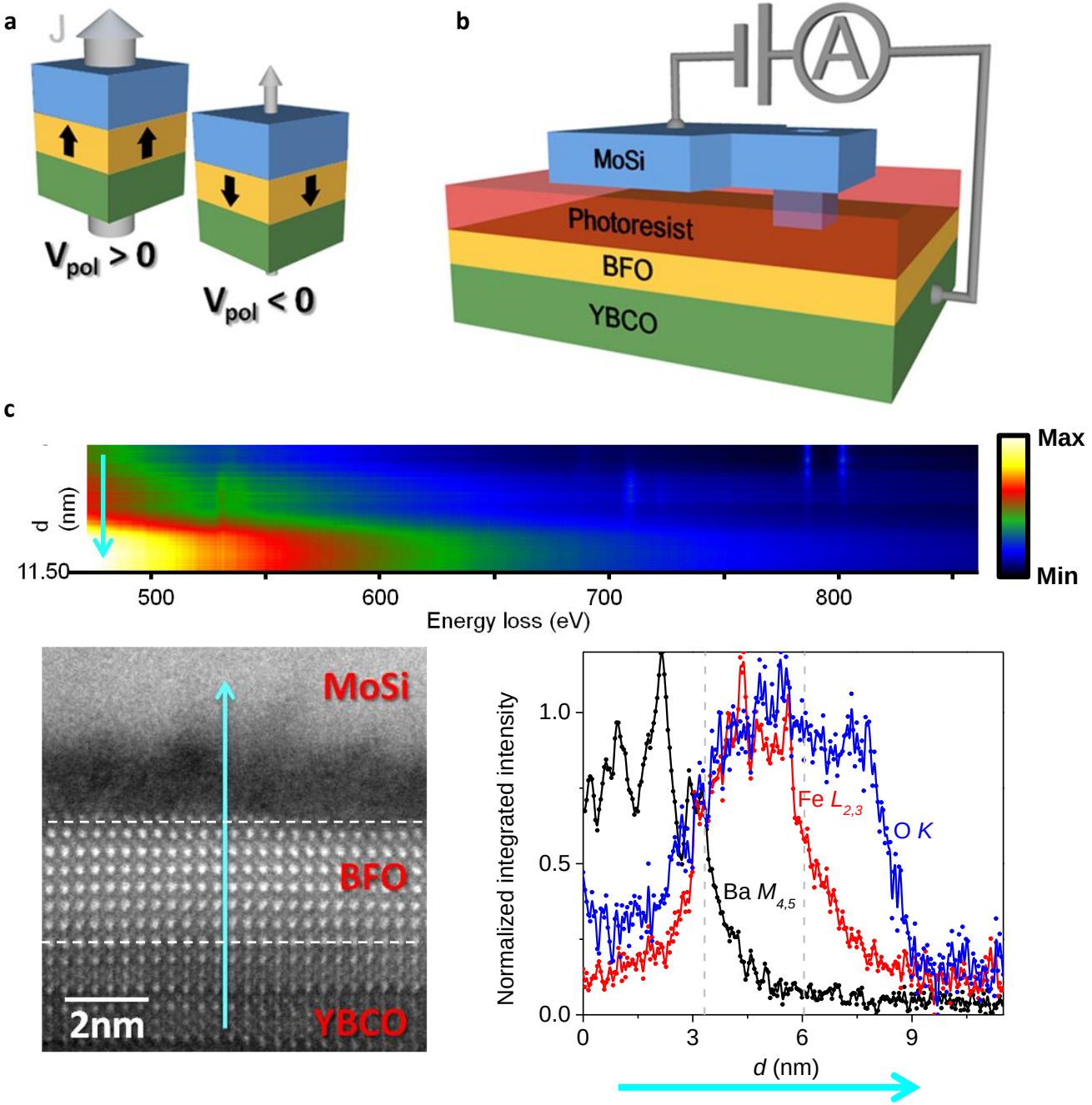
a
J
$V_{pol} > 0$
$V_{pol} < 0$
b
A
MoSi
Photoresist
BFO
YBCO
c
d (nm)
11.50
500
600
700
800
Energy loss (eV)
Max
Min
MoSi
BFO
YBCO
2nm
Normalized integrated intensity
1.0
0.5
0.0
0
3
6
9
d (nm)
Fe $L_{2,3}$
O K
Ba $M_{4,5}$

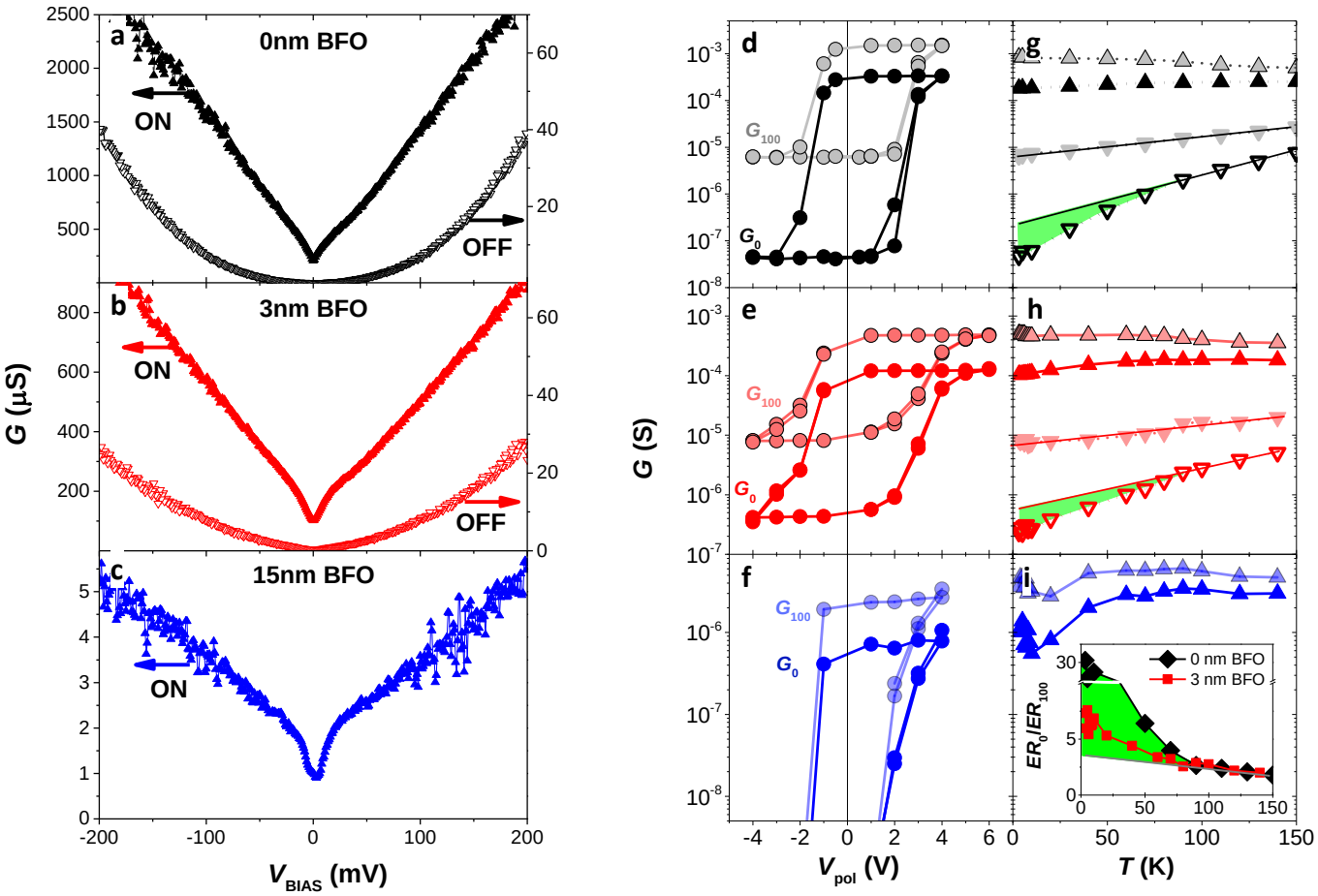
a
0nm BFO
ON
OFF
b
3nm BFO
ON
OFF
c
15nm BFO
ON
G (μS)
V_BIAS (mV)
d
e
f
g
h
i
G_100
G_0
G (S)
V_pol (V)
T (K)
0 nm BFO
3 nm BFO
ER_0/ER_100

Figure 2

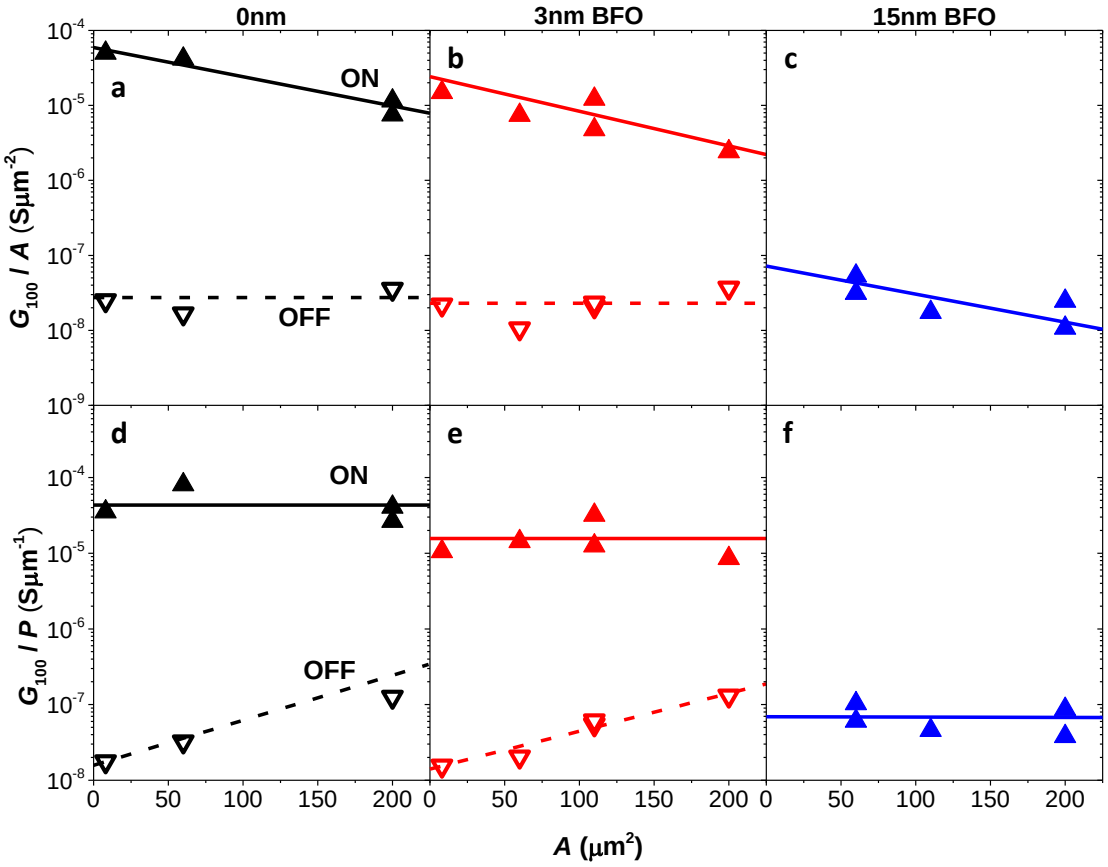
0nm
3nm BFO
15nm BFO
a
b
c
d
e
f
ON
OFF
ON
OFF
G_{100} / A (Sμm^{-2})
G_{100} / P (Sμm^{-1})
A (μm^2)
10^{-4}
10^{-5}
10^{-6}
10^{-7}
10^{-8}
10^{-9}
0
50
100
150
200

Figure 3

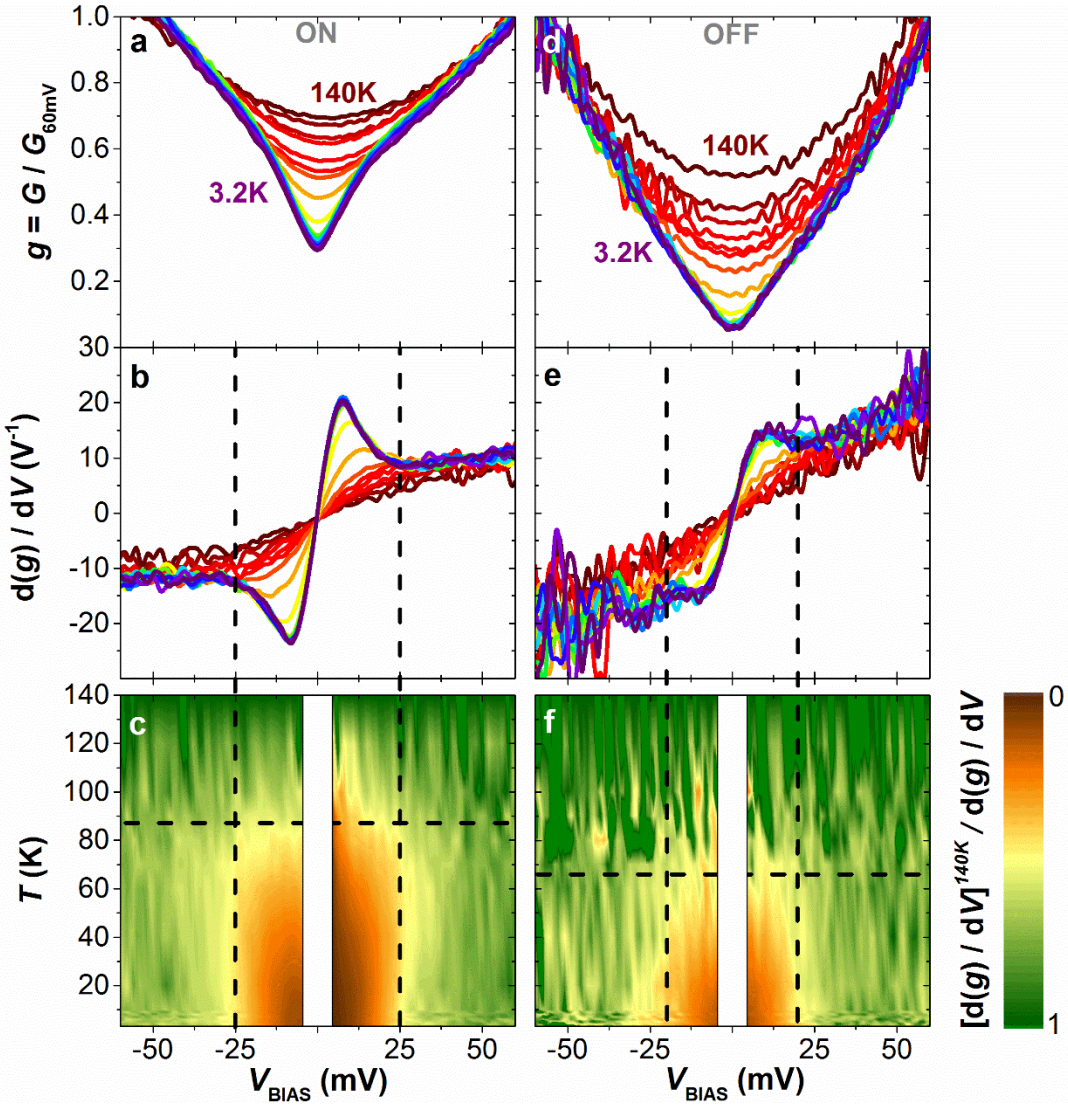
a
ON
140K
3.2K
d
OFF
140K
3.2K
g = G / G60mV
b
e
d(g) / dV (V-1)
c
f
T (K)
VBIAS (mV)
VBIAS (mV)
[d(g) / dV]140K / d(g) / dV
0
1

Figure 4

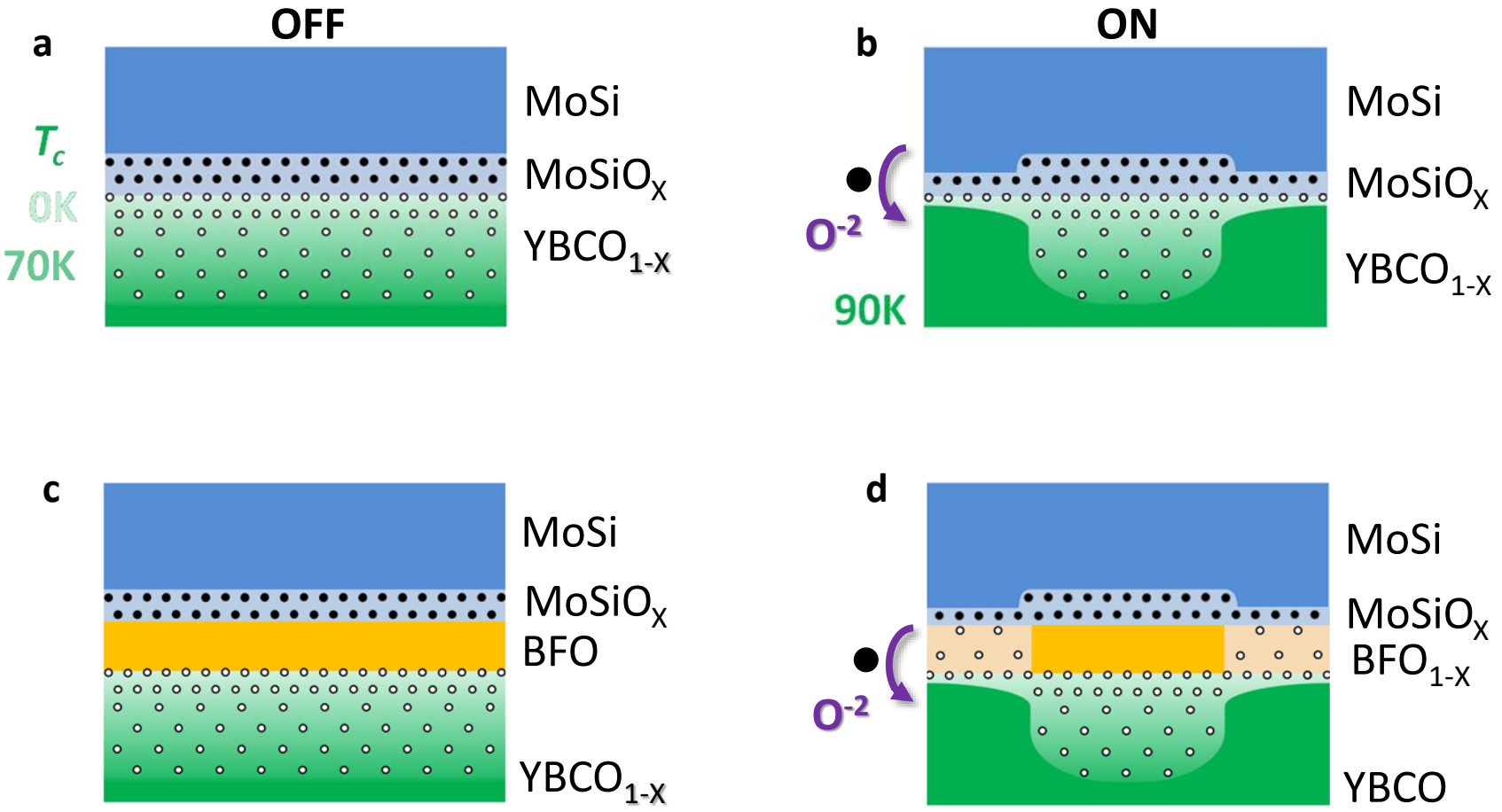
a
OFF
T_c
0K
70K
MoSi
$MoSiO_X$
$YBCO_{1-X}$
b
ON
O^{-2}
90K
MoSi
$MoSiO_X$
$YBCO_{1-X}$
c
MoSi
$MoSiO_X$
BFO
$YBCO_{1-X}$
d
O^{-2}
MoSi
$MoSiO_X$
BFO_{1-X}
YBCO

Figure 5

SUPPLEMENTARY INFORMATION FOR

"Quasiparticle Tunnel Electroresistance in Superconducting Junctions"

V. Rouco[1], R. El Hage[1] , A. Sander[1], J. Grandal[2], K. Seurre[1], X. Palermo[1], J. Briatico[1], S. Collin[1], J. Trastoy[1], K. Bouzehouane[1], A.I. Buzdin[3], G. Singh[4], N. Bergeal[4], C. Feuillet-Palma[4], J. Lesueur[4], C. Leon[2], M. Varela[2], J. Santamaría[1,2] and Javier E. Villegas[1]

[1]*Unité Mixte de Physique, CNRS Thales, Université Paris-Sud, Université Paris Saclay, 91767 Palaiseau, France*

[2]*Grupo de Física de Materiales Complejos, Dpt. Física de Materiales, Universidad Complutense de Madrid, 28040 Madrid, Spain*

[3]*Univ Bordeaux, LOMA UMR CNRS 5798, F-33405 Talence, France*

[4]*Laboratoire de Physique et d'Etude des Matériaux, ESPCI Paris, Université PSL, CNRS, 75005 Paris (France)*

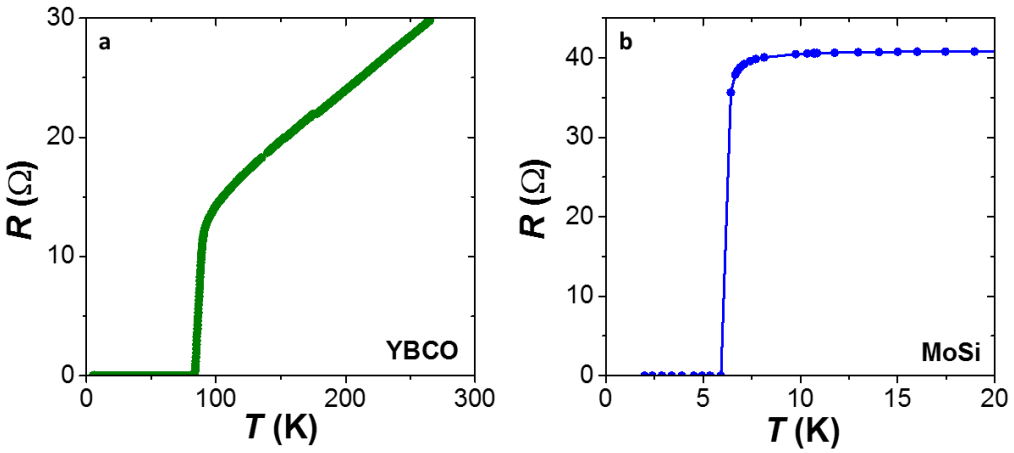

Supplementary Figure 1: Superconducting properties of the electrodes. 4-probe resistance measurement of (a) YBCO and (b) MoSi electrodes, measured with a current I = 10 μA. The onset of the superconducting transition is observed at T_C ~91 K for YBCO and T_C ~ 6.8K for MoSi**.**

Material	Reduction reaction	Reduction potential E_0 (V)
YBCO	$Cu^{+3} + e^{+} \rightarrow Cu^{+2}$	2.4
BFO	$Fe^{+3} + e^{+} \rightarrow Fe^{+2}$	0.7
$Mo_{80}Si_{20}$	$Mo^{+3} + 3e^{-} \rightarrow Mo$	-0.2
$Mo_{80}Si_{20}$	$Si^{+2} + 2e^{-} \rightarrow Si$	-0.8
ITO (In_2O_3 98%/SnO_2 2%)	$In^{+3} + + e - \rightarrow In+2$	-0.49

Supplementary Table 1: Reduction potentials of the junction materials. Obtained from the *Table of Standard Electrode Potentials* by Milazzo et al., edited by Willey (Chichester), 1978. For YBCO and BFO, we have considered the change of valence of Cu and Fe expected[1,2] when oxygen is removed from the structure. For MoSi we quote the two elements Mo and Si, and for ITO we select In since In_2O_3 constitutes 98% (weight) of the material. Data for $SrTiO_3$ not available as the expected reduction $Ti^{+4} + e - \rightarrow Ti^{+3}$ is not tabulated. We see from the table that YBCO has the highest reduction potential. Thus, the redox reaction through which oxygen is transferred into the counter-electrode (MoSi or ITO) is expectedly spontaneous. The voltage required to reverse this reaction equals ΔE_0, which lies between 2.6 and 3.2 V in all cases.

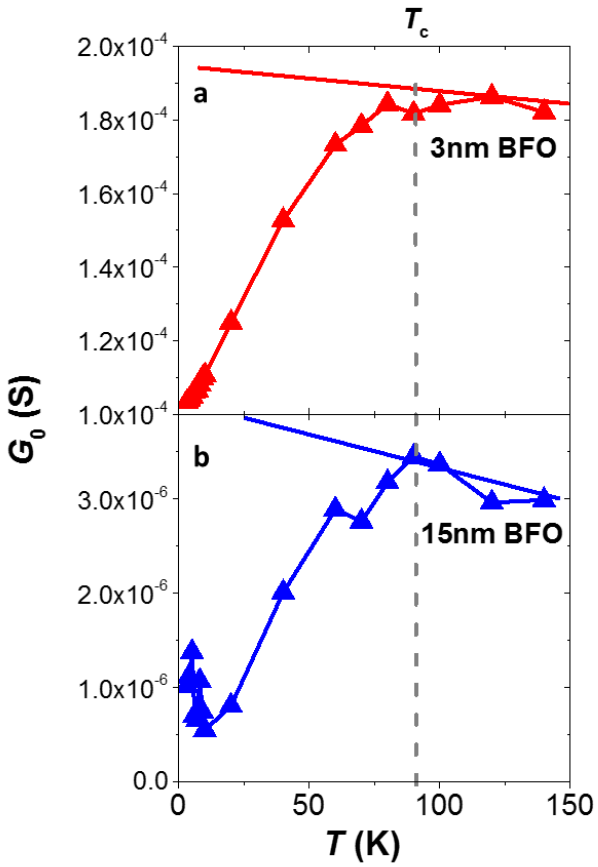

Supplementary Figure 2: Zero bias conductance vs. temperature in the ON state. G_0 data shown in Figs. 2h and 2i, here displayed in linear scale to enable appreciation of the temperature at which $G_0(T)$ departs from the high-temperature trend indicated by the straight lines. The temperature is approximately the T_C of optimally doped YBCO, as pointed by the vertical dashed line.

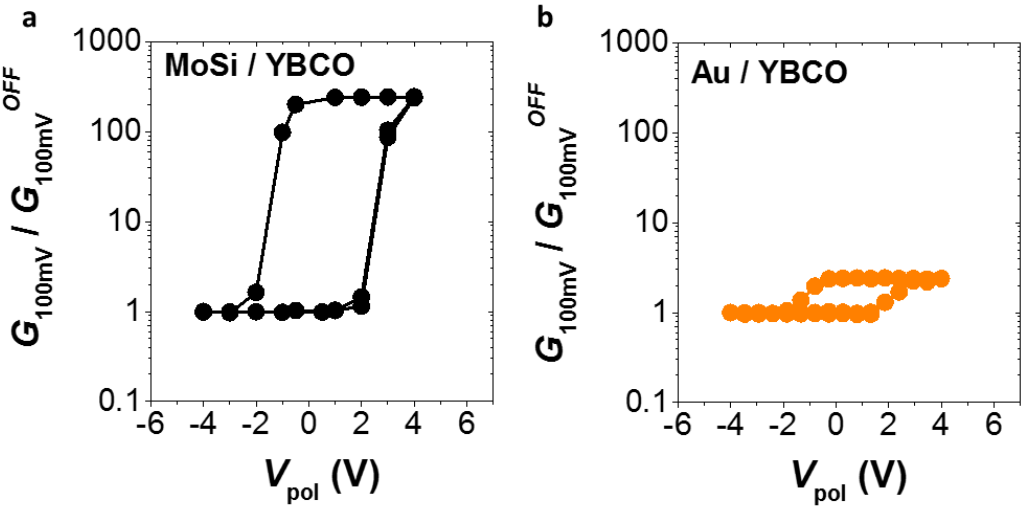

Supplementary Figure 3: Conductance switching for direct contacts: comparison between YBCO/MoSi and YBCO/Au junctions. Conductance switching measured at 100 mV in (a) a MoSi/YBCO junction and in (b) Au/YBCO junction of the same area (200µm^2). One can see that the conductance changes more than two orders of magnitude in the first case, but only a factor of ~2 in the second, as expected from earlier experiments in Au/YBCO contacts[3]. This very different behaviour demonstrates that a metal with tendency to oxidize (MoSi) is required to obtain large conductance switching comparable with the TER of ferroelectric tunnel junctions.

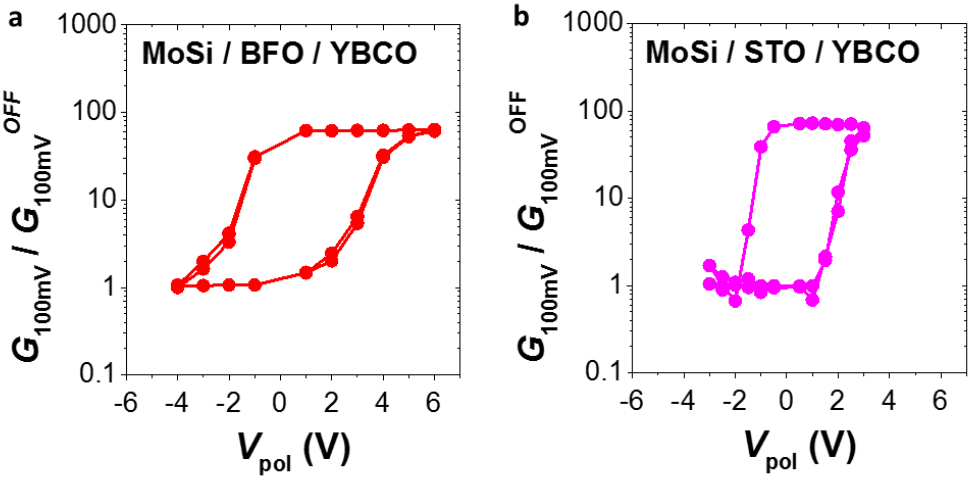

Supplementary Figure 4: Conductance switching for junctions with different barriers: comparison between ferroelectric (BFO) and non-ferroelectric (STO) barriers. Conductance switching measured at 100 mV in (a) a MoSi/BFO_{3nm}/YBCO junction and in (b) MoSi/STO_{3nm}/YBCO junction of the same area (200µm^2). $SrTiO_3$ is a non-ferroelectric band insulator. One can see that the conductance switching is qualitatively and quantitatively similar in both types of junctions, which shows that the ferroelectric character of BFO is not playing a major role in the conductance switching behaviour.

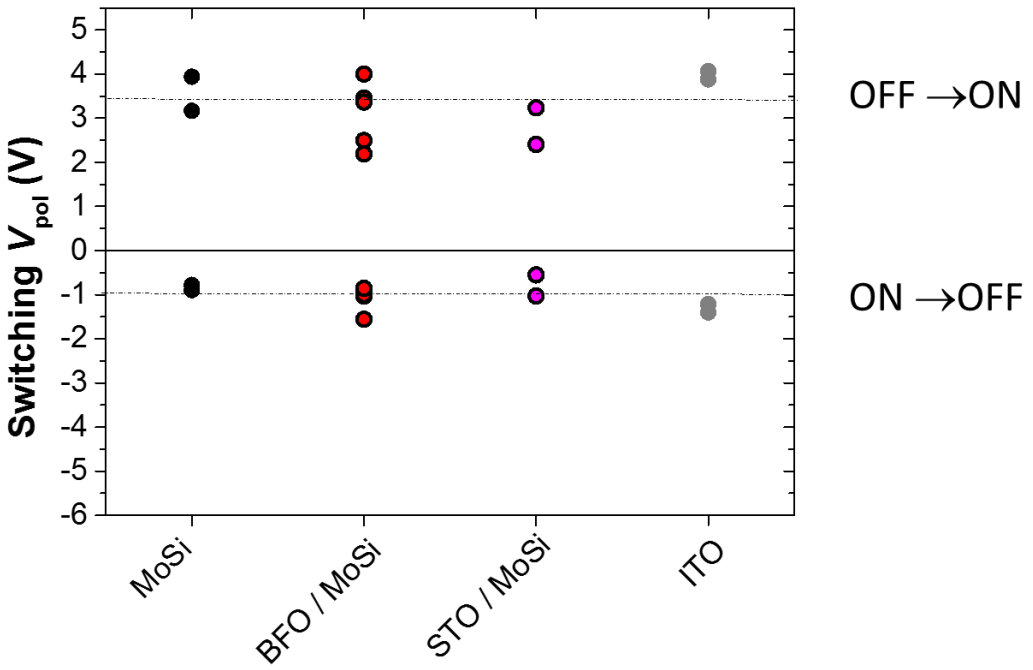

Supplementary Figure 5: Switching voltages for different types of junctions. Voltages V_{pol} for switching from the OFF into the ON state ($V_{pol} > 0$) and vice versa ($V_{pol} > 0$) for different types of junctions in which the conductance switching size is similar (around two orders of magnitude at 100 mV). The different types of junctions include direct contacts between $Mo_{80}Si_{20}$ (MoSi) or In_2O_3/SnO_2 (ITO) and YBCO, as well as junctions in which an interlayer is placed in between MoSi and YBCO, particularly $BiFeO_3$ (BFO) and $SrTiO_3$ (STO). For all these junctions, the switching voltages are defined as the voltage for which $\left(G_{100\mathrm{mV}} - {G_{100\mathrm{mV}}}^{OFF}\right)/{G_{100\mathrm{mV}}}^{ON}$ = 0.5. One can see that, within the experimental error given by the data scattering for each type of junction (several devices were measured in each case), the switching V_{pol} are rather similar for all junctions. Notice the asymmetry, with V_{pol} (ON→OFF)~-1V and V_{pol} (ON→OFF) ~ 3.5 V. The latter is similar to the difference between reduction potential of the junction electrodes, ΔE_0, as calculated in section 2 above.

Supplementary Note 1: Estimates of tunnelling barrier height and width from fits to BDR model.

In order to estimate the tunnel junction parameters, we fitted the conductance curves $G(V_{BIAS})$ in the normal state (T = 90K) to the Brinkman, Dynes, and Rowell (BDR) model[7].

$$\frac{G(V)}{G(0)} = 1 - \left(\frac{A_0 \Delta\varphi}{16\varphi^{\frac{3}{2}}}\right) eV + \left(\frac{9}{128}\frac{{A_0}^2}{\varphi}\right)(eV)^2 \qquad (1)$$

where $\Delta\varphi$ is the barrier asymmetry, φ is the average barrier height, and $A_0 = 4(2m)^{1/2}d/3\hbar$ with m the electron mass and d the tunnel barrier thickness.

We have only studied the curves in the OFF state at low bias (< 100 mV), where the conductance shows a parabolic dependence. Fitting of the ON states curves to this model is not possible since the nearly linear conductance background $G \propto |V_{BIAS}|$ indicates the predominance of inelastic tunneling[4].

The fit shown for 0 nm YBCO yields an energy barrier 0.15 ± 0.02 eV, a total barrier thickness 5.0 ± 0.2 nm, and a barrier asymmetry ~ 20% of the barrier height. The fit for the 3 nm BFO film is for a barrier width 8.0 ± 0.5 nm, in consistency with the above result for 0 nm BFO. That barrier width implies a barrier height 0.53±0.03 eV.

We show in Supplementary Figure 7 a scheme of the tunnel barrier as deduced from the above fits.

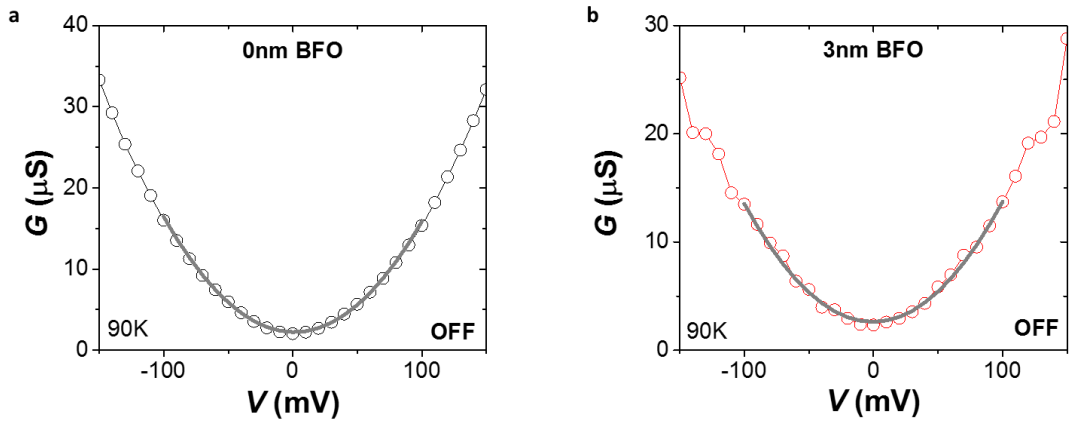

Supplementary Figure 6: Fits of the normal-state tunnelling conductance to the BDR model for junctions with 0 nm BFO and 3 nm BFO

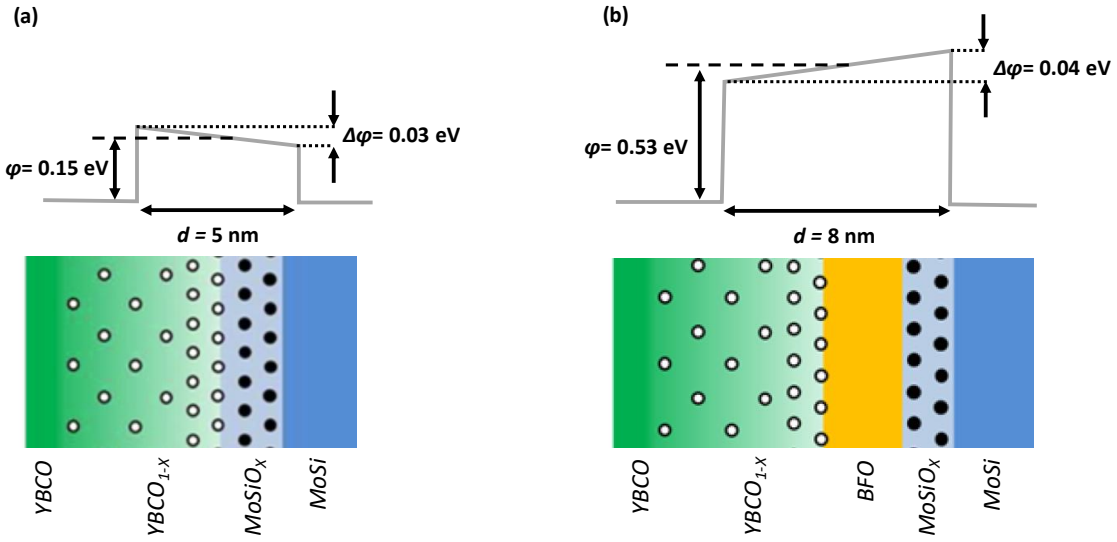

Supplementary Figure 7: Scheme of the energy barrier across the tunnel junction without BFO **(a)** and with **(b)** 3 nm BFO.

Supplementary Note 2: Estimates of the barrier strength through simulations with the BTK theory.

Besides drastically varying in the junctions' resistance, the switching between the ON and OFF states produces spectral changes in the differential conductance $g(V)$. These changes can be analysed in the frame of the Blonder-Tinkham-Klapwijk (BTK)[7] theory for superconductor/metal junctions, which explains the conductance features associated to the superconducting gap(Δ) through a parameter *Z* that measures the junction's barrier strength (the higher *Z*, the lower the junction transparency).

The insets of Supplementary Figure 8 (a) and (b) respectively show the normalized conductance $g_S(V)/g_N(V)$ in the ON and OFF state, with $g_S(V)$ measured in the superconducting state (at *T*=3.2 K) and $g_N(V)$ measured just above T_C. One can see that the gap-related "dip" around zero bias is deeper in the OFF than in the ON state. Within the BTK theory, this can be interpreted as Z being higher in the OFF that in the ON state, which is consistent with the junction resistance being much higher in the OFF that in the ON state.

We carried out a more quantitative analysis using the BTK theory extended to the case of c-axis tunnelling into d-wave superconductors[8,9]. Because the BTK theory does not account for the temperature and bias dependence of the background conductance (evident in the experiments for $eV>>\Delta$), comparison between the BTK conductance and the experiments requires removing the (weak) quadratic background highlighted by the magenta dotted lines in the insets of Supplementary Figure 8. For this, we re-normalize $g_S(V)/g_N(V)$ to the background, which yields the data shown in the main panel of Supplementary Figure 8 (black dots). These data are to be compared to the simulations made with the BTK theory (coloured lines).

We fist attempted fitting the bare BTK theory[8,9] to the experimental data, by fixing the value of Δ according to the analysis in Fig. 4 and varying *Z*. Examples of the calculated BTK conductance are depicted with blue lines in Supplementary Figure 8 (a) and (b). One can see that the

experimental curves show a strong smearing of coherence peaks near the gap edge as compared with the bare BTK theory. In order to improve the fits, we considered broadening effects, in particular the effect of finite quasiparticle lifetime[10,11] (which can be quantified by means of a phenomenological parameter Γ) as well as the presence of inhomogeneity in the properties of the superconductor[12]. The red solid lines show a simulations including those effects, particularly by considering[10,11] Γ=3 mV and averaging over 50 simulations with a standard deviation of the gap of σ_Δ=5 mV in order to simulate the effect of inhomogeneity. One can see that this allows a better fit to the experimental results.

Besides providing further support to the interpretation of the tunnelling conductance spectra given in the main text, the above analysis provides a solid estimate of the barrier strength *Z* in the ON and OFF states, respectively Z_{ON}~3 and Z_{OFF}~30.

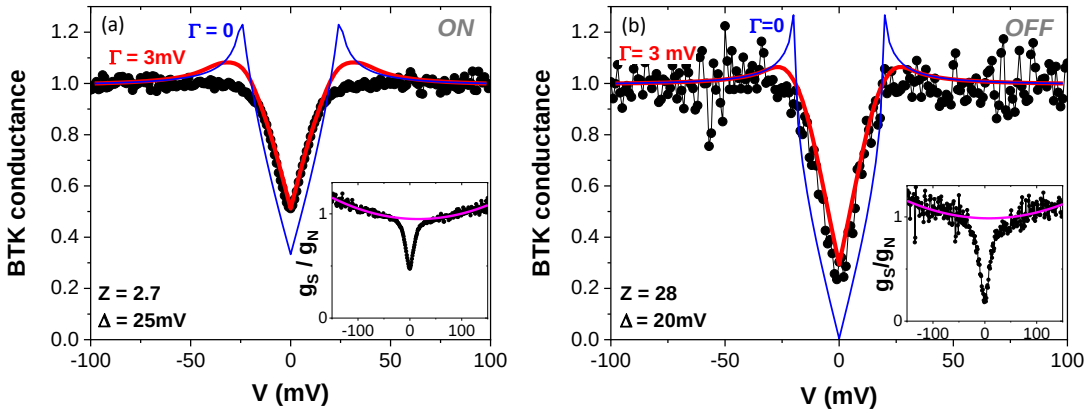

Supplementary Figure 8: Analysis of the conductance using the BTK theory. For a 3nm BFO sample. In the ON state (a) in the OFF one (b). Experimental data are depicted by black dots and theoretical simulations by lines (blue and red). The values for the parameters *Z* and Δ, and the different values of inelastic scattering parameter Γ are indicated in the legend. of Insets: show the conductance in the superconducting state g_S(measured at 3.2 K) normalized to the normal-state conductance g_N (measured right above T_C, at *T*=90 K in the ON state and *T*=70 K in the OFF state). The weak background dependence highlighted by the pink dotted line is obtained from a fit of $g_S(V)/g_N(V)$ to a quadratic polynomial in the range 30mV<|V|<100. mV), and that is removed for the BTK analysis in the main panel.

Supplementary Note 3: Modelling of the temperature dependent tunnelling electro-resistance via BTK theory.

The simulations of differential conductance *vs.* bias at different temperatures shown in Fig. 5 were calculated with the generalized BTK theory[8,9], in which temperature effects are included through the Fermi-Dirac function and the temperature dependence of superconducting gap $\Delta(T) = \Delta_0 \tanh\left(2.06\sqrt{T_C/T-1}\right)$ generally considered for d-wave superconductors[13]. We performed calculations both for the ON and OFF states [see examples in Fig. 5a using the parameters obtained in Supplementary Note 3 (we assume that Γ is temperature independent

as elsewhere[13]). From the calculations, we extracted the BTK conductance at zero-bias (G_0) and at 100 mV (G_{100}) as a function of temperature, which is shown in Fig. 5b. Note that for clarity we have multiplied the BTK conductance by a factor G_{100} that is different in the ON and OFF, thus mimicking the ON/OFF conductance switching. Notice finally that, as discussed in Supplementary Note 3, the BTK theory does not account for the temperature and bias dependence of the background conductance. Consequently, although the BTK simulations reproduce the main features of the bias and temperature dependent ER, they do not account for the temperature dependent G_{100} observed experimentally, and cannot perfectly reproduce the experimental ER_0/ER_{100} vs. T.

Supplementary references

1. Temmerman, W. M., Winter, H., Szotek, Z. & Svane, A. Cu valency change induced by O doping in YBCO. *Phys. Rev. Lett.***86**, 2435–2438 (2001).

2. Sæterli, R., Selbach, S. M., Ravindran, P., Grande, T. & Holmestad, R. Electronic structure of multiferroic BiFeO3 and related compounds: Electron energy loss spectroscopy and density functional study. *Phys. Rev. B - Condens. Matter Mater. Phys.***82**, 29–33 (2010).

3. Plecenik, A. *et al.* Influence of bias voltage history on conductance properties of YBaCuO/normal metal junctions. *Phys. C Supercond. its Appl.***301**, 234–242 (1998).

4. Kirtley, J., Washburn, S. & Scalapino, D. Origin of the linear tunneling conductance background. *Phys. Rev. B. Condens. Matter***45**, 336–346 (1992).

5. Boyn, S. *et al.* Engineering ferroelectric tunnel junctions through potential profile shaping. *APL Mater.***3**, (2015).

6. Tzung-Lin Li *et al.* Novel dual-metal gate technology using Mo-MoSi/sub x/ combination. *IEEE Trans. Electron Devices***53**, 1420–1426 (2006).

7. Blonder, G. E., Tinkham, M. & Klapwijk, T. M. Transition from metallic to tunneling regimes in superconducting microconstrictions: Excess current, charge imbalance, and supercurrent conversion. *Phys. Rev. B***25**, 4515–4532 (1982).

8. Kashiwaya, S., Tanaka, Y., Koyanagi, M., Takashima, H. & Kajimura, K. Origin of zero-bias conductance peaks in high-Tc superconductors. *Phys. Rev. B***51**, 1350 (1995).

9. Wei, J. Y. T., Yeh, N. C., Garrigus, D. F. & Strasik, M. Directional tunneling and andreev reflection on YBa2Cu3O7 − δ single crystals: Predominance of d-wave pairing symmetry verified with the generalized blonder, tinkham, and klapwijk theory. *Phys. Rev. Lett.***81**, 2542–2545 (1998).

10. Dynes, R. C., Narayanamurti, V. & Garno, J. P. Direct Measurement of Quasiparticle-Lifetime Broadening in a Strong-Coupled Superconductor. *Phys. Rev. Lett.***41**, 1509–1512 (1978).

11. Plecenník, A., Grajcar, M., Beňačka, Š., Seidel, P. & Pfuch, A. Finite-quasiparticle-lifetime effects in the differential conductance of Bi 2 Sr 2 CaCu 2 O y /Au junctions. *Phys. Rev. B***49**, 10016–10019 (1994).

12. Feigel'man, M. V. & Skvortsov, M. A. Universal Broadening of the Bardeen-Cooper-

Schrieffer Coherence Peak of Disordered Superconducting Films. *Phys. Rev. Lett.***109**, 147002 (2012).

13. Park, W. K., Greene, L. H., Sarrao, J. L. & Thompson, J. D. Andreev reflection at the normal-metal/heavy-fermion superconductor Ce Co In 5 interface. *Phys. Rev. B***72**, 052509 (2005).